catalysts

MDPI

Article

High-Efficiency Oxygen Reduction to Hydrogen Peroxide Catalyzed by Oxidized Mo_2TiC_2 MXene

Ge Li, Bin Zhou, Ping Wang, Miao He, Zhao Fang, Xilin Yuan, Weiwei Wang, Xiaohua Sun * and Zhenxing Li *

State Key Laboratory of Heavy Oil Processing, College of New Energy and Materials, China University of Petroleum (Beijing), Beijing 102249, China; superligelige@163.com (G.L.); wenwubin2@163.com (B.Z.); wpingnib@163.com (P.W.); hemiao9603@163.com (M.H.); fangzhaost@163.com (Z.F.); 13156296206@163.com (X.Y.); weiweiwang_work@163.com (W.W.)

* Correspondence: hua82@126.com (X.S.); lizx@cup.edu.cn (Z.L.)

Abstract: The two-electron oxygen reduction reaction ($2e^-$ORR) pathway electrochemical synthesis to H_2O_2 has the advantages of low investment and environmental protection and is considered to be a promising green method. Herein, the oxidized Mo_2TiC_2 MXene (O-Mo_2TiC_2) was successfully synthesized by a facile hydrothermal method as an electrocatalyst in electrocatalytic H_2O_2 production. The O-Mo_2TiC_2 achieved the 90% of H_2O_2 selectivity and 0.72 V vs. RHE of the onset potential. Moreover, O-Mo_2TiC_2 showed high charge transfer ability and long-term stable working ability of 40 h. This significantly enhanced electrocatalytic H_2O_2 production capacity is assigned the oxidation treatment of Mo_2TiC_2 MXene to generate more oxygen-containing groups in O-Mo_2TiC_2. This work provides a promising catalyst candidate for the electrochemical synthesis of H_2O_2.

Keywords: two-electron oxygen reduction reaction; electrochemical H_2O_2 production; Mo_2TiC_2 MXene; oxidation treatment

check for updates

Citation: Li, G.; Zhou, B.; Wang, P.; He, M.; Fang, Z.; Yuan, X.; Wang, W.; Sun, X.; Li, Z. High-Efficiency Oxygen Reduction to Hydrogen Peroxide Catalyzed by Oxidized Mo_2TiC_2 MXene. *Catalysts* **2022**, *12*, 850. https://doi.org/10.3390/catal12080850

Academic Editors: Lichen Bai and Jun Gu

Received: 14 July 2022
Accepted: 1 August 2022
Published: 2 August 2022

1. Introduction

Hydrogen peroxide (H_2O_2) is a green and crucial oxidant that has been widely used in the chemical industry, environmental remediation, and textile manufacturing [1–3]. Currently, the industrial production of H_2O_2 mainly relies on the energy-intensive anthraquinone technology, which is a multi-step process that not only requires complex and large-scale facilities but also generates large amounts of waste chemicals [4–6]. In addition, the high-concentration H_2O_2 may pose high cost and safety issues during storage and transportation [7–10]. In fact, in most applications, only diluted H_2O_2 (0.1–3% $g{\cdot}L^{-1}$) is required [11–13]. For these reasons, it is an emerging trend to develop an energy-efficient route that reduces the cost of H_2O_2 synthesis, storage, and transportation [14–17]. Recently, the electrochemical generation of H_2O_2 from the oxygen reduction reaction (ORR) via a $2e^-$ transfer has attracted the attention of the academic community [18–21]. Besides, the electrochemical generation of H_2O from the ORR via a $4e^-$ transfer is the crucial pathway in fuel cell applications and metal-air batteries [22–26]. Therefore, the development of highly selective and performance $2e^-$ ORR electrocatalysts is the prerequisite for producing H_2O_2 [27–29].

For this purpose, noble metal and alloy catalysts have been verified to have high ORR activity and H_2O_2 selectivity, such as Pt, Pd, and Au-based catalysts [6,30,31]. However, their high cost and scarcity hinder their large-scale applications [32,33]. So far, two-dimensional (2D) carbon-based materials have shown good performance in the electrochemical synthesis of H_2O_2 due to their abundant reserve, tunable electronic structures, and composition versatility [34–37]. Recently, researchers have been developing other potential electrocatalysts, such as MXenes, which are two-dimensional metal carbides or nitrides [38–40]. MXenes are considered promising catalysts for the generation of H_2O_2 via $2e^-$ transfer [41–45].

MXenes have recently attracted great attention in the field of electrocatalysis due to their tunable composition and excellent chemical properties [35,46,47]. For instance, Yury et al. used Mo_2TiC_2Tx to support Pt single atom, showing excellent hydrogen evolution reaction (HER) performance [48]. Additionally, Xiao Huang et al. prepared $Ti_3C_2T_x$, V_2CT_x, and Nb_2CT_x for H_2O_2 electrosynthesis and found that MXenes are inherent $2e^-$ORR catalysts with high H_2O_2 selectivity [42]. Not only that, MXenes can be used in other applications. For instance, Tang et al. found that the MXenes and their fluorinated/hydroxylated derivative materials were advantageous materials for Li-ion battery applications [49]. Additionally, Xu et al. also developed a strategy to prepare rGO/Ti_3C_2Tx electrodes using Ti_3C_2Tx as the active conductive binder between rGO nanosheets [50]. Apart from this, Li et al. reported MXene quantum dots and graphitic carbon nitride nanosheets for the preparation of heterostructured $g\text{-}C_3N_4@Ti_3C_2$ quantum dots, which showed improved photocatalytic ability [51]. It can be seen that MXenes have a wide range of applications; however, its research of $2e^-$ORR in the electrochemical synthesis of H_2O_2 should be further strengthened.

In the present work, we have developed a facile synthetic method for preparing oxidized Mo_2TiC_2 MXene ($O\text{-}Mo_2TiC_2$) catalysts. $O\text{-}Mo_2TiC_2$ materials provide high selectivity and are active in the electrochemical synthesis of hydrogen peroxide under alkaline conditions. Catalyst evaluation for different pH environments also reveals that pH has an effect on performance. Furthermore, the electrocatalytic H_2O_2 production performance of the catalyst is indeed affected by the variation of catalyst loading on the working electrode, which has been demonstrated. This study opens up new directions in search of more active and selective electrocatalysts for the efficient production of H_2O_2.

2. Results and Discussion

The preparation of the $O\text{-}Mo_2TiC_2$ is schematically demonstrated in Scheme 1. Firstly, the Mo_2TiAlC_2 was added into hydrofluoric acid to etch Al to obtain a layered Mo_2TiC_2 MXene, which was further exfoliated by adding tetrabutylammonium hydroxide. Finally, the $O\text{-}Mo_2TiC_2$ was obtained via hydrothermal treatment with high concentrations of potassium hydroxide.

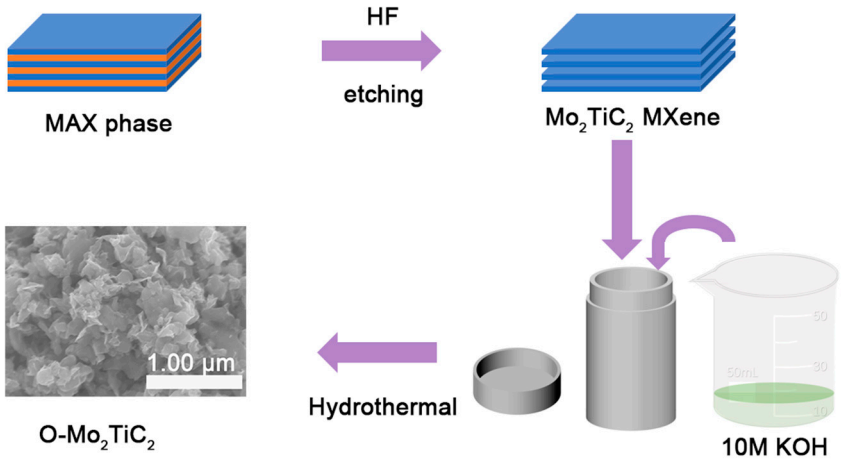

Scheme 1. Schematic illustration of $O\text{-}Mo_2TiC_2$ preparation process.

To investigate the structural features of Mo_2TiAlC_2, Mo_2TiC_2 MXene, and $O\text{-}Mo_2TiC_2$, we performed X-ray diffraction (XRD) analysis on these three materials (Figure 1a,b). Compared with Mo_2TiAlC_2, the (002) diffraction peak of Mo_2TiC_2 MXene has shifted to a lower angle (2θ from 9° to 7°), indicating that the interlayer spacing increases after the addition of tetrabutylammonium hydroxide. In addition, there is a characteristic weak peak of the (004) crystal plane, which is consistent with the formation of the MXene phase. As shown in Figure 1b, the diffraction peaks of MoO_3 and TiO_2 are observed in $O\text{-}Mo_2TiC_2$,

which is consistent with literature reports [52–55], indicating the successful synthesis of oxidized Mo_2TiC_2. According to Figure S1, compared with the Mo_2TiC_2 EDX spectrum, there is no Al peak in the Mo_2TiC_2 MXene, indicating that the aluminum element was completely removed during the etching process. Figure 1c,d depict the morphology of the O-Mo_2TiC_2 forming process. As shown in Figure 1c, Mo_2TiC_2 MXene has obvious layered and sheet-like structures. The morphology and structure of O-Mo_2TiC_2 synthesized by the hydrothermal method did not change in Figure 1d. Compared with the Mo_2TiC_2 MXene, the O-Mo_2TiC_2 still maintains the corresponding layered structure, indicating that the layered structure and crystallinity of Mo_2TiC_2 MXene are hardly influenced by the oxidation process. In order to further determine the morphology and structural characteristics of Mo_2TiC_2 MXene and O-Mo_2TiC_2, we also carried out transmission electron microscopy (TEM) analysis, and the analysis results are shown in Figure 1e,f. It can be seen from the TEM images that the O-Mo_2TiC_2 and Mo_2TiC_2 MXene maintain a nearly similar layered structure.

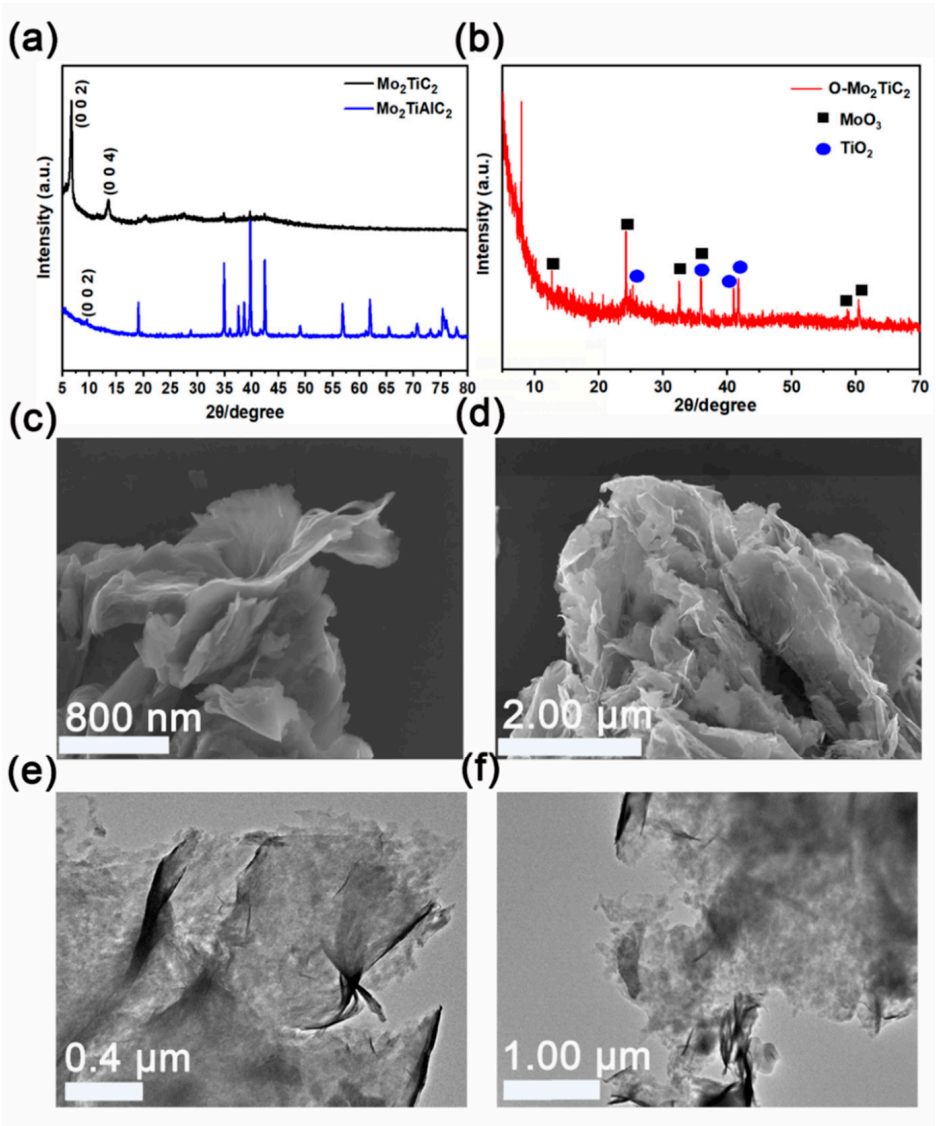

Figure 1. (**a**) XRD spectra of Mo_2TiC_2 MXene and Mo_2TiAlC_2. (**b**) XRD spectra of O-Mo_2TiC_2. SEM images of (**c**) Mo_2TiC_2 MXene and (**d**) O-Mo_2TiC_2. TEM images of (**e**) Mo_2TiC_2 MXene and (**f**) O-Mo_2TiC_2.

In order to verify the distribution of C, O, Ti, and Mo, we used energy dispersive X-ray spectrometer (EDX) elemental mapping to analyze the O-Mo_2TiC_2. In Figure 2a–g, we can clearly see that the distribution of C, O, Ti, and Mo in the O-Mo_2TiC_2 is very uniform, indicating that the O element has been successfully introduced into the O-Mo_2TiC_2. The elemental contents (atomic %) for EDX analysis is: C = 38.70%, O = 31.95%, Ti = 9.91%, Mo = 19.45%, and the mass ratio: C = 14.01 wt%, O = 15.41 wt%, Ti = 14.31 wt%, Mo = 56.27 wt%. The specific surface areas of Mo_2TiC_2 MXene and O-Mo_2TiC_2 were measured via N_2 adsorption–desorption in Figure 2h, and the Brunauer–Emmett–Teller (BET) specific surface area is 5.41 m^2 g^{-1} and 12.80 m^2 g^{-1}, respectively, suggesting that the oxidation process is in favor of improving the specific surface area of Mo_2TiC_2 MXene. The Raman spectra of the O-Mo_2TiC_2 are recorded in Figure 2i. Raman modes can be observed at around 170, 245, 310, and 770 cm^{-1} in all samples [56]. These modes closely match previous reports on the Raman spectra of Mo_2TiC_2, giving further evidence of the successful synthesis of Mo_2TiC_2. It has been reported that the peak around 170 cm^{-1} results from the Eg vibration of both Mo and Ti atoms, and the peak at around 245 cm^{-1} corresponds directly to the Eg vibration of the O atoms, which suggests the presence of Mo-O in this MXene. The peaks at 310 and 770 cm^{-1} are all thought to mostly originate from the vibrations of C atoms in the MXene. The sharp bands at 385 and 442 cm^{-1} correspond to Raman active modes of TiO_2 [57]. The presence of Mo-O bands can be confirmed since its characteristic main bands at 282,666 and 710 cm^{-1} (A_g) cm^{-1} are observed, which is in accordance with previous analysis [57–59].

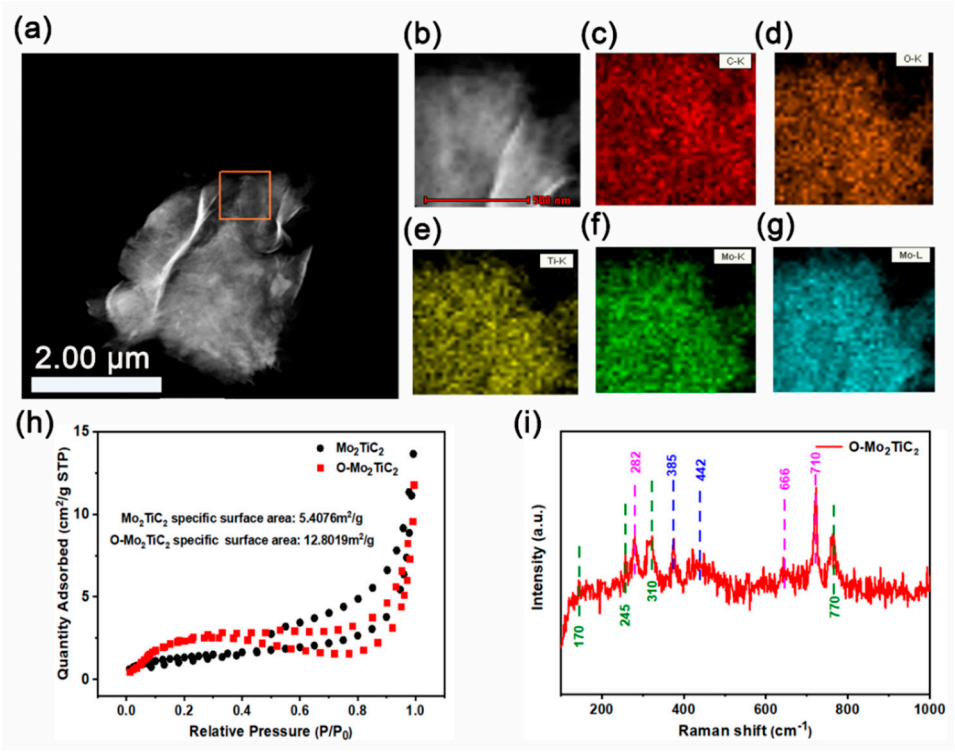

Figure 2. (**a**–**g**) EDX elemental mapping images of C, O, Ti, and Mo in O-Mo_2TiC_2. (**h**) N_2 adsorption–desorption isotherms for Mo_2TiC_2 MXene and O-Mo_2TiC_2. (**i**) Raman spectra of O-Mo_2TiC_2.

We also conducted X-ray photoelectron spectroscopy (XPS) analysis of the Mo_2TiC_2 MXene and O-Mo_2TiC_2, from which the chemical composition and valence state of each element during the oxidation reaction could be determined, which clearly confirmed the surface functional groups of the samples before and after the reaction. The XPS survey spectrum (Figure 3a,b) shows the presence of O, Ti, C, and Mo as the main components of Mo_2TiC_2 MXene and O-Mo_2TiC_2.

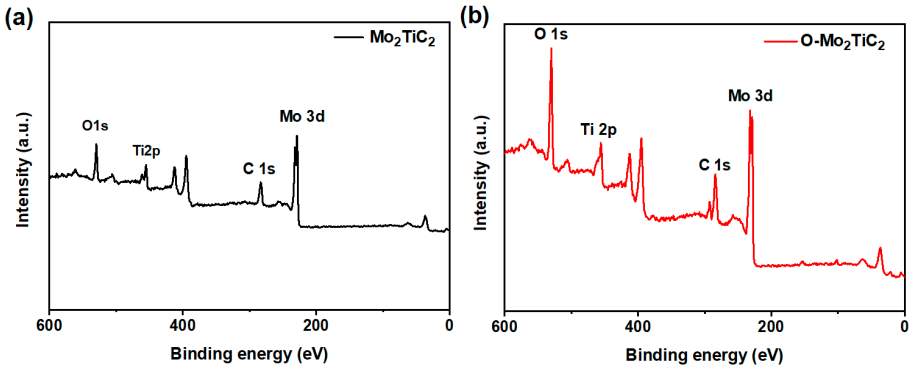

Figure 3. (**a**,**b**) XPS survey spectra of Mo_2TiC_2 and O-Mo_2TiC_2.

Figures S2 and 4a–d show the high-resolution XPS spectra of Mo_2TiC_2 MXene and O-Mo_2TiC_2, where the changes of C 1s, Mo 3d, Ti 2p, and O 1s before and after the oxidation process are clearly observed. The three peaks of C 1s are C-O (286.1 eV), C-C (384.5 eV), and Mo(Ti)-C (282.0 eV) in Figure S2a [56]. Mo 3d has peaks of Mo-C (234.3 eV and 231.1 eV) and Mo-Ox (237.4 eV and 234.7 eV) in Figure S2b [56]. The three peaks of Ti 2p are Ti-O (458.9 eV), Ti-C (463.4 eV and 457.4 eV) in Figure S2c [56]. The three peaks of O 1s are Mo_2TiC_2-OH (531.4 eV), Mo_2TiC_2-Ox (529.9 eV), and Mo(Ti)-Ox (529.0 eV) in Figure S2d [56]. For O-Mo_2TiC_2 in Figure 4a–d, C 1s is mainly a new peak COO (288.3 eV) and an increase in C-O (285.6 eV) content in Figure 4a [48]. Figure 4b,c show that the original oxygen-containing peak areas of the other two elements also increased to varying degrees, and new oxygen-containing peaks also increased. After the oxidation treatment, the new peaks of Mo-Ox (235.3 eV and 232.0 eV in Figure 4b) and Ti-Ox (463.7 eV in Figure 4c) were introduced [44]. We can conclude that the oxidation process of O-Mo_2TiC_2 introduces more oxygen-containing groups. These oxygen-containing groups, including Mo-Ox and Ti-Ox, are important for the electrocatalytic process. Therefore, both Mo and Ti are important for the electrocatalytic process.

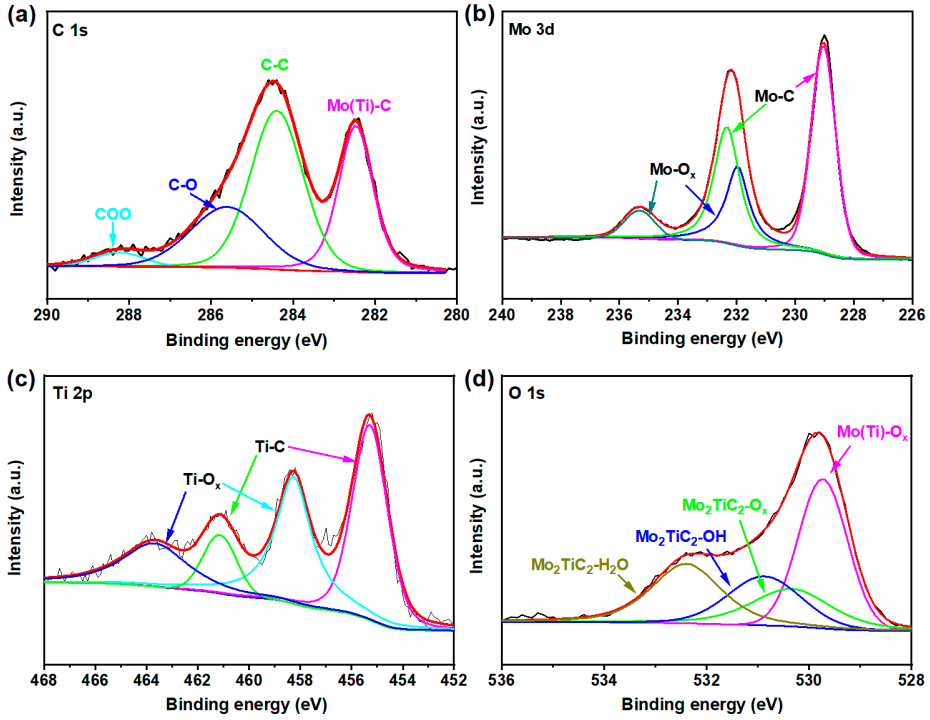

Figure 4. High-resolution XPS spectra of O-Mo_2TiC_2: (**a**) C 1s, (**b**) Mo 3d, (**c**) Ti 2p, and (**d**) O 1s.

The electrocatalytic H_2O_2 production activity of the as-prepared O-Mo_2TiC_2 was evaluated by cyclic voltammetry (CV) in alkaline and neutral electrolytes, respectively, in Figure S3. Figure S3a shows almost no characteristic curve in the N_2-saturated 0.1 M KOH solution, while a distinct reduction peak appears in the O_2-saturated 0.1 M KOH solution (Figure S3b). Moreover, similar CV test results can also be observed in neutral solutions (Figure S3c,d), indicating that the O-Mo_2TiC_2 has a remarkable electrocatalytic activity for oxygen reduction. Especially in 0.1 M KOH electrolyte, the reduction peak is very obvious, indicating that the ORR activity is significantly enhanced in an alkaline solution. Following the above results, we evaluated the electrocatalytic activity of the O-Mo_2TiC_2 using an RRDE. Because the ORR can be divided into $4e^-$pathway and $2e^-$pathway, the electrocatalytic production of H_2O_2 is a typical $2e^-$ORR pathway. To study the electrocatalytic H_2O_2 production capability of O-Mo_2TiC_2 under both alkaline and neutral conditions, we employed two electrolytes: 0.1 M KOH solution (pH~13) and 0.1 M Na_2SO_4 solution (pH~7). Figures 5a and S4 show the electrochemical results of the catalysts in the two electrolytes (the rotation speed of the RRDE electrode at 1600 rpm), where the oxygen reduction current (solid line) was measured on the disk electrode, and the H_2O_2 oxidation current (dotted line) were measured on platinum ring electrodes. According to Figures 5a and S4, whether in 0.1 M KOH solution or 0.1 M Na_2SO_4 solution, compared with Mo_2TiC_2 MXene, O-Mo_2TiC_2 has a stronger ability to electrochemically synthesize H_2O_2, that is, higher ring current and corrected onset potential (0.1 M KOH solution: 0.72 V vs. RHE; 0.1 M Na_2SO_4 solution: 0.33 V vs. RHE). Therefore, combined with the above analysis, the electrocatalytic activity of Mo_2TiC_2 for H_2O_2 production is much higher than that of Mo_2TiC_2 MXene. This is because the surface oxidation treatment makes Mo_2TiC_2 MXene generate more oxygen-containing functional groups, which greatly increases the active sites of the reaction and improves the electrocatalytic ability of the catalyst O-Mo_2TiC_2 to produce H_2O_2.

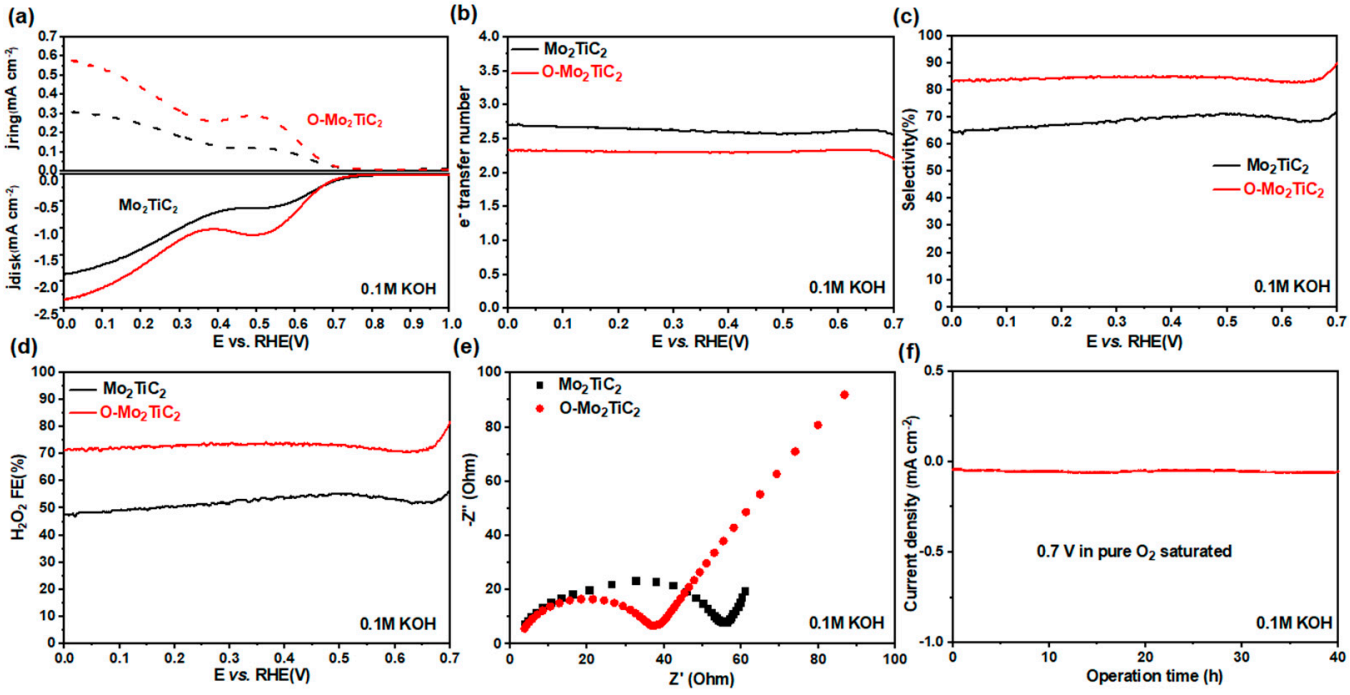

Figure 5. (**a**) Polarization curves (solid line) and H_2O_2 detection current densities (dashed lines) at the ring electrode for Mo_2TiC_2 MXene and O-Mo_2TiC_2t at 1600 rpm in 0.1 M KOH solution. (**b**–**d**) Transfer electron number, H_2O_2 selectivity, and Faradaic efficiency of Mo_2TiC_2 MXene and O-Mo_2TiC_2 in 0.1 M KOH solution. (**e**) Nyquist plots of catalysts O-Mo_2TiC_2 and Mo_2TiC_2 MXene in 0.1 M KOH solution. (**f**) Stability test of catalyst O-Mo_2TiC_2 in 0.1 M KOH solution for 40 h.

As shown in Figure 5b, the number of transferred electrons of O-Mo_2TiC_2 is closer to $2e^-$. Therefore, O-Mo_2TiC_2 is easier to carry out the $2e^-$ORR process so as to achieve the purpose of H_2O_2 production. The H_2O_2 selectivity of O-Mo_2TiC_2 is maintained above 83% (Figure 5c), and the H_2O_2 selectivity reached the peak of 90% at 0.7 V vs. RHE, which is much higher than the highest H_2O_2 selectivity (70%) of Mo_2TiC_2 MXene. Similar results were observed in neutral solution (0.1 M Na_2SO_4 solution). The H_2O_2 selectivity of O-Mo_2TiC_2 reached 83% (Figure S5), which is higher than the 59% selectivity of Mo_2TiC_2 MXene in a neutral solution. Moreover, the number of transferred electrons also confirms this result in Figure S6. We also calculated the Faradaic efficiency (FE) of H_2O_2 in a 0.1 M KOH solution; the FE of O-Mo_2TiC_2 is 81% at 0.7 V vs. RHE (Figure 5d), which is much higher than Mo_2TiC_2 MXene (56%). The FE of O-Mo_2TiC_2 (Figure S7) is 70% in 0.1 M Na_2SO_4 solution, which is also much higher than the 42% of Mo_2TiC_2 MXene. Therefore, the above results indicate that the O-Mo_2TiC_2 exhibits a higher electrocatalytic H_2O_2 production capacity than the Mo_2TiC_2 MXene in both neutral and alkaline solutions. The impedance and interfacial electron transfer ability of O-Mo_2TiC_2 and Mo_2TiC_2 MXene in alkaline solution and neutral solution were analyzed via electrochemical impedance spectroscopy (EIS). According to Figures 5e and S8, O-Mo_2TiC_2 showed lower charge transfer resistance, indicating the better electrochemical performance and fast dynamics, and the EIS fitting results are shown in Table S1. The internal resistance (R_1) is consistent, while the transfer resistance (R_2) is smaller than that of Mo_2TiC_2 MXene. Therefore, it is indicated that the O-Mo_2TiC_2 achieves a fast faradaic process and excellent reaction kinetics due to the introduction of oxygen element, which is consistent with the above-mentioned results of H_2O_2 activity and selectivity analysis. The stability is an important basis for studying whether the catalyst can be commercialized. Combined with the above analysis and test results, the O-Mo_2TiC_2 exhibited a high electrocatalytic ability to produce H_2O_2 in 0.1 M KOH solution. Therefore, we mainly tested the stability of O-Mo_2TiC_2 in an alkaline solution. As shown in Figure 5f, the O-Mo_2TiC_2 can continue to work for 40 h under the voltage of 0.7 V vs. RHE, and no obvious overpotential change is observed. Therefore, the O-Mo_2TiC_2 show good stability and great potential for large-scale practical application, which makes O-Mo_2TiC_2 a promising candidate catalyst to further enhance the potential of electrocatalytic H_2O_2 production at the industrial level.

The effects of loading amount on the H_2O_2 selectivity were also investigated in alkaline and neutral solutions (Figures 6a and S9). The LSV curves of ring current and disk current in alkaline solution are consistent with the neutral solution. The onset potential of the LSV curve is the highest when the O-Mo_2TiC_2 loading is 50 μg cm^{-2} and the H_2O_2 oxidation current is the highest. In alkaline solution, the different loadings of O-Mo_2TiC_2 have obvious effects on the number of transferred electrons, H_2O_2 selectivity, and Faradaic efficiency in Figures 6b–d and S10–S12. With the decrease in the O-Mo_2TiC_2 loading, the ability of $2e^-$ORR to produce H_2O_2 gradually increased, the number of transferred electrons gradually approached $2e^-$, and the H_2O_2 selectivity and Faradaic efficiency also gradually increased. In 0.1 M KOH solution, when the catalyst loading gradually decreased, the number of transferred electrons gradually approached $2e^-$ (from $3.2e^-$ to $2e^-$) in Figure 6b, the H_2O_2 selectivity was gradually increased from 41% to 90% (Figure 6c), and the FE increased gradually from 25% to 80% (Figure 6d). Similar to an alkaline solution, when the catalyst loading was gradually decreased in neutral solution, the number of transferred electrons gradually approached $2e^-$ (from 3.4 e^- to $2.3e^-$) in Figure S10, and the H_2O_2 selectivity gradually increased from 32% to 83% (Figure S11), and the FE increased gradually from 19% to 70% (Figure S12). Based on the above experimental results, the O-Mo_2TiC_2 loading was very low, such as 50 μg cm^{-2}, and the O-Mo_2TiC_2 showed lower $4e^-$ORR activity and higher H_2O_2 activity. Therefore, we believe that when the O-Mo_2TiC_2 layer is very thin, the generated H_2O_2 would quickly escape from the active site of the O-Mo_2TiC_2 layer and avoid being further reduced.

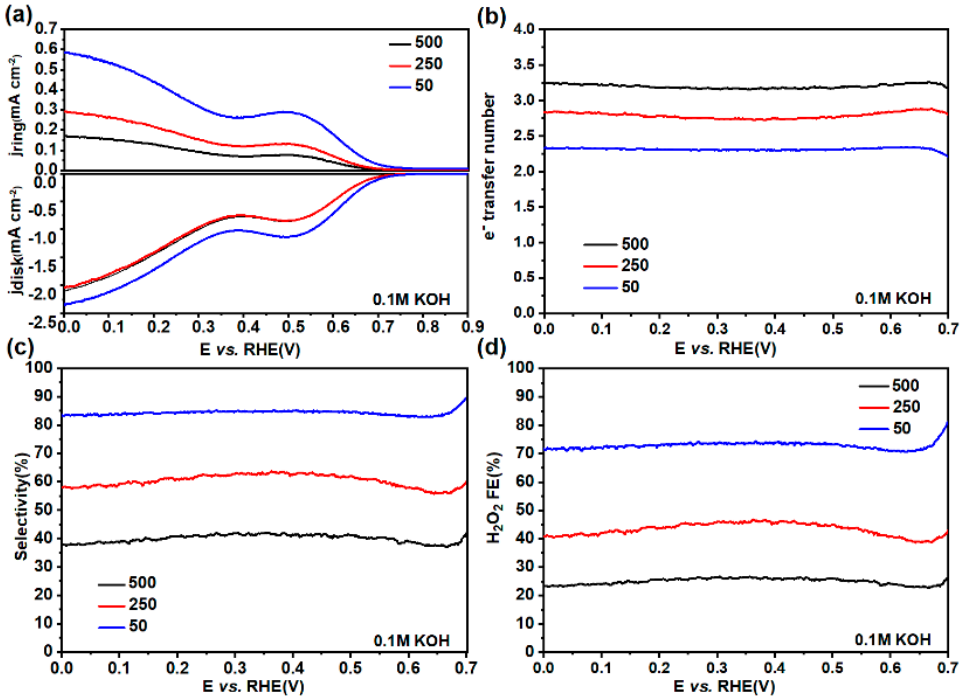

Figure 6. (**a**) Different loadings of O-Mo_2TiC_2: LSV curves in 0.1 M KOH solution at 1600 rpm. (**b**–**d**) Transfer electron number, H_2O_2 selectivity, and Faradaic efficiency of O-Mo_2TiC_2 with different loadings in 0.1 M KOH solution.

In order to verify the effect of thickness on catalytic performance, we tested the electrocatalytic performance of O-Mo_2TiC_2 with a larger thickness. Figure S13 shows an SEM image of O-Mo_2TiC_2 with a thicker thickness. The test results are shown in Figures S14–S17. Comparing the results of Figures S14–S17 with Figures 5a–d and 6a–d, it can be seen that the thicker O-Mo_2TiC_2 has a lower ring current and smaller onset potential (onset potential: 0.64 V vs. RHE). The H_2O_2 selectivity of the thicker thickness O-Mo_2TiC_2 is 41% in Figure S15, which is lower than that of the thinner thickness O-Mo_2TiC_2. In addition, the results of the number of transferred electrons (3.2 e^-) in Figure S16, and the Faradaic efficiency (25%) in Figure S17, were calculated. Combined with the above analysis, the electrocatalytic activity of the thinner O-Mo_2TiC_2 for H_2O_2 production is much higher than that of the thicker O-Mo_2TiC_2. The reason is that the thinner O-Mo_2TiC_2 provides more reaction sites, greatly improving the electrocatalytic activity of O-Mo_2TiC_2.

3. Materials and Methods

3.1. Reagents and Chemicals

Potassium hydroxide (KOH, AR) was purchased from Shanghai McLean (Shanghai Aladdin Biochemical Technology Co., Ltd, Shanghai, China), aqueous hydrofluoric acid (HF, 40 wt%) was purchased from Fuchen (Fuchen Chemical Reagent Co., Ltd, Tianjin, China), carbon-aluminum-titanium-molybdenum (Mo_2TiAlC_2, AR) was purchased from Yiyi Technology (Jilin Province Yiyi Technology Co., Ltd, Jilin, China), argon gas (High purity) from Beijing Millennium (Beijing Millennium Jingcheng Gas Co., Ltd, Beijing, China), and tetrabutylammonium hydroxide ($C_{16}H_{37}NO$, 40 wt%) was purchased from Energy Chemical (Sarn Chemical Technology Co., Ltd, Shanghai, China). The ultrapure water used in all experiments was purified with a Milli-Q system.

3.2. Synthesis of Mo_2TiC_2 MXene and O-Mo_2TiC_2

3.2.1. Synthesis of Mo_2TiC_2 MXene

Mo_2TiAlC_2 (1 g) powder was slowly added to 40 wt% HF (20 mL), and the solution was stirred in an oil bath at 55 °C for 72 h. After 72 h, the solution was cooled at room

temperature and then washed and centrifuged with deionized water continuously. The multilayered Mo_2TiC_2 MXene powder was collected when the decanted supernatant pH was neutral. The as-synthesized dry multilayer Mo_2TiC_2 MXene powder was dispersed into 60 mL of deionized water, and then, 1 mL of 40 wt% tetrabutylammonium hydroxide (TBAOH) was added. After sonication for 1 h under the continuous flow of argon and centrifugation at 3000 rpm for half an hour, the supernatant in the test tube was collected to obtain a layered Mo_2TiC_2 MXene solution. The solution was frozen overnight in a refrigerator and dried with a freeze dryer to obtain a layered Mo_2TiC_2 MXene powder, which was collected and frozen for later use.

3.2.2. Synthesis of Oxidized Mo_2TiC_2-Based MXene Materials

In this experiment, the hydrothermal method was used to prepare the oxidized Mo_2TiC_2-based MXene material; that is, the Mo_2TiC_2 MXene powder was oxidized with a high concentration (10 M) KOH solution in a polytetrafluoroethylene kettle. Briefly, about 50 mg of the previously prepared Mo_2TiC_2 powder was dispersed in 40 mL of 10 M KOH solution, stirred by ultrasonic for 30 min, and then transferred to an oven for 12 h at 180 °C. After 12 h, the product solution was naturally cooled to room temperature and then washed and centrifuged with deionized water and absolute ethanol continuously. When the pH of the poured supernatant was neutral, the product was transferred to a vacuum drying oven at 60 °C for about 10 h to dry it completely. The prepared sample is simply referred to as O-Mo_2TiC_2 in the rest of the paper.

3.3. Characterization of Mo_2TiC_2 MXene and O-Mo_2TiC_2

Scanning electron microscopy (SEM) measurements were performed with a Hitachi SU8010 scanning electron microscope at 200 kV. Transmission electron microscopy (TEM) was measured with a Tecnai F20 at 200 kV. Wide-angle X-ray diffraction (XRD) was performed with a Burker D8-advance X-ray diffractometer (operating current: 40 mA, operating voltage: 40 KV) under Cu-Kα (λ = 0.15406 nm) radiation. X-ray photoelectron spectroscopy (XPS) was measured with Mg-KR radiation (BE) at 1253.6 eV. Nitrogen adsorption–desorption isotherms were measured with a micromertics ASAP 2460 analyzer (USA) at liquid nitrogen temperature (77 K), and the samples were measured after degassing in a vacuum at 80 °C for 6 h. The surface area was obtained using the Brunauer–Emmett–Teller (BET) method. Raman spectra were collected using a Raman spectrometer (HORIBA labRAM HR Evolution).

3.4. Electrochemical Performance Tests

The tests on electrocatalytic hydrogen peroxide (H_2O_2) production in this paper were all completed by a CHI760E electrochemical workstation and rotating disk electrode device. The working electrode was a rotating ring disk electrode (RRDE) assembly (AFE7R9GCPT, Pine Research Instrumentation Inc, Shanghai, China) composed of a glassy carbon rotating disk electrode (area: 0.196 cm^2) and a platinum ring, with a theoretical collection efficiency of 35%. The counter electrode is a carbon rod, and the reference electrode is Hg/HgO electrode. Test in normal temperature and pressure environment, test two different electrolytes: 0.1 M KOH solution (alkaline, "pH = 13") and 0.1 M Na_2SO_4 solution (neutral, "pH = 7").

In order to ensure the accuracy of the experiment, we determined the collection efficiency of the RRDE electrode used by a specific experiment, that is, measuring the RRDE electrode in a nitrogen-saturated solution of 1 M KNO_3 and 10 mM $K_3Fe(CN)_6$ (Macklin, AR, >99.5%) Apparent collection efficiency (N) in as shown in Figure S18 the apparent collection efficiency N was 34.3% at 1600 rpm. Because the apparent collection efficiency of the RRDE electrode is only related to the electrode itself and has nothing to do with other conditions such as catalyst and electrolyte, the measured data (N = 34.3%) can be directly used in subsequent experiments.

Here is a full description of the experiment:

(1) Catalyst preparation:

Add 600 µL ultrapure water, 400 µL absolute ethanol, and 10 µL Nafion solution (5 wt%) to a 2 mL centrifuge tube. Another 5 mg of catalyst was weighed and mixed with it. Sonicate for half an hour to form a uniform ink and be ready to use. Use a pipette to drop the ink onto a glass carbon disk (surface area 0.196 cm^2, the catalyst loading can be adjusted at any time according to the experimental needs, about 500 µg cm^{-2}~50 µg cm^{-2}), and dry at room temperature. On the glassy carbon disk electrode, the catalyst layer is uniform with no obvious pinholes or exposed edges.

(2) RRDE measurement:

Before the electrochemical performance test, in order to eliminate the air in the electrolyte as much as possible, it is necessary to ventilate the electrolyte with N_2 for 30 min. Then, the cyclic voltammetry (CV) curve was tested at a scan rate of 50 $mV{\cdot}s^{-1}$, with at least 40 cycles until the CV curve remained stable. Then ventilate the electrolyte with O_2 for 30 min. After that, the cycle was repeated 20 times at a scan rate of 10 $mV{\cdot}s^{-1}$ until the CV curve remained stable. Finally, the linear sweep voltammogram (LSV) in the O_2-saturated electrolyte was measured by polarization curves and a rotating ring disk electrode (RRDE). The ORR polarization curve was saved by adjusting the rotating disk electrode device to keep the electrode rotation speed at 1600 rpm and the scan rate at 10 $mV{\cdot}s^{-1}$ for measurement.

To detect the generated H_2O_2 while avoiding other ORR currents, the Pt ring potential was kept at 1.4 V vs. RHE during LSV. All LSV curves were corrected with resistance compensation and potential scales given relative to a reversible hydrogen electrode (RHE).

From the disc current (ID) and ring current (IR) results, determine the H_2O_2 selectivity and transfer number of electrons (n) with the following formulas:

$$H_2O_2\% = 200\frac{I_R/N}{I_D + I_R/N} \quad (1)$$

$$n = 4\frac{I_D/N}{I_D + I_R/N} \quad (2)$$

The formula for calculating the Faradaic efficiency (FE) of H_2O_2:

$$\text{Faradaic efficiency of } H_2O_2\% = 100\frac{I_R/N}{|I_D|} \quad (3)$$

(3) Electrochemical impedance spectroscopy (EIS) was acquired in the range of 106 Hz to 0.1 Hz, measured in an oxygen-saturated 0.1 M KOH aqueous solution at 0.65 V vs. RHE. All measurement potentials using the three-electrode setup are manually 100% compensated.

(4) The stability of the catalyst in this experiment was tested by the potentiostatic method, and the catalyst was tested under fixed voltage conditions for 40 h (0.7 V vs. RHE).

3.5. Mechanism

The $2e^-$ORR pathway for H_2O_2 production proceeds through Equations (4) and (5):

$$O_2 + H_2O + e^- \rightarrow OOH* + OH \quad (4)$$

$$OOH* + e^- \rightarrow HO_2^- \quad (5)$$

First, hydrogenation of oxygen occurs on active sites via proton-electron transfer to form OOH* intermediate, and then, OOH* intermediate is reduced to HO_2^- with second electron transfer. Therefore, the OOH* intermediate plays a key role in the $2e^-$ORR for H_2O_2 formation, and the adsorption energy of OOH* is used as the descriptor to evaluate the catalytic activity of different active sites [60,61].

4. Conclusions

Mo_2TiC_2 MXene was synthesized using hydrofluoric acid as an etchant and then oxidized with a high concentration of KOH solution by hydrothermal method to obtain O-Mo_2TiC_2. The H_2O_2 selectivity of O-Mo_2TiC_2 in alkaline solution reached up to 90%, and the onset potential reached 0.72 V vs. RHE. Moreover, O-Mo_2TiC_2 exhibited high charge transfer ability and long-term stable working ability (40 h). The significantly enhanced electrocatalytic H_2O_2 production is mainly due to the oxidation treatment of Mo_2TiC_2 MXene to generate more oxygen-containing groups in O-Mo_2TiC_2, which are beneficial to the improvement of electrocatalytic H_2O_2 production performance via increasing the active sites. It was also found that the electrocatalytic H_2O_2 production performance of the catalysts was indeed affected by the variation of the catalyst loading on the working electrode. This work provides a promising catalyst for the electrochemical synthesis of H_2O_2.

Supplementary Materials: The following supporting information can be downloaded at: https://www.mdpi.com/article/10.3390/catal12080850/s1, Figure S1: TEM-EDAX patterns of Mo_2TiC_2 MXene and O-Mo_2TiAlC_2; Figure S2: High-resolution XPS spectra of Mo_2TiC_2 MXene (a) C 1s, (b) Mo 3d, (c) Ti 2p, and (d) O 1s; Figure S3: CV curves of O-Mo_2TiC_2 in two different electrolytes, with a scan rate of 50 mV s^{-1}; 0.1 M KOH solution: (a) saturated with N_2, (b) saturated with O_2; 0.1 M Na_2SO_4 solution: (c) N_2 saturated, (d) O_2 saturated; Figure S4: Polarization curves (solid line) and H_2O_2 detection current densities (dashed lines) at the ring electrode for Mo_2TiC_2 MXene and O-Mo_2TiC_2t at 1600 rpm in 0.1 M Na_2SO_4 solution; Figure S5: H_2O_2 selectivity of Mo_2TiC_2 MXene and O-Mo_2TiC_2 in 0.1 M Na_2SO_4 solution; Figure S6: Transfer electron number of Mo_2TiC_2 MXene and O-Mo_2TiC_2 in 0.1 M Na_2SO_4 solution; Figure S7: Faradaic efficiency of Mo_2TiC_2 MXene and O-Mo_2TiC_2 in 0.1 M Na_2SO_4 solution; Figure S8: Nyquist plots of catalysts Mo_2TiC_2 MXene and O-Mo_2TiC_2 in 0.1 M Na_2SO_4 solution; Figure S9: Different loadings of O-Mo_2TiC_2 LSV curves in 0.1 M Na_2SO_4 solution at 1600 rpm; Figure S10: Number of transferred electrons of O-Mo_2TiC_2 with different loadings in 0.1 M Na_2SO_4 solution; Figure S11: H_2O_2 selectivity of O-Mo_2TiC_2 with different loadings in 0.1 M Na_2SO_4 solution; Figure S12: Faradaic efficiency of O-Mo_2TiC_2 with different loadings in 0.1 M Na_2SO_4 solution; Figure S13. SEM image of O-Mo_2TiC_2 with thicker thickness; Figure S14. LSV curves of O-Mo_2TiC_2 with thicker thickness in 0.1M KOH; Figure S15. H_2O_2 selectivity of O-Mo_2TiC_2 with thicker thickness in 0.1 M KOH; Figure S16. Number of transferred electrons of O-Mo_2TiC_2 with thicker thickness in 0.1 M KOH; Figure S17. Faradaic efficiency of O-Mo_2TiC_2 with thicker thickness in 0.1M KOH; Figure S18: Collection efficiency of pure RRDE electrodes: N = 34.3%; Table S1: EIS data obtained by fitting the experimental data, R_1 is the simulated internal resistance, R_2 is the charge transfer resistance.

Author Contributions: X.S. and Z.L. conceived the project and designed the experiments. G.L., B.Z., and P.W. performed the experiments. M.H. carried out material characterization. Z.F. assisted in material characterization. X.Y. and W.W. wrote the manuscript. All authors have read and agreed to the published version of the manuscript.

Funding: This research was funded by the National Key Research and Development Program of China (Grant No. 2021YFB4000405) and the National Nature Science Foundation of China (Grant No. 22122113).

Data Availability Statement: The data presented in this study are openly available.

Conflicts of Interest: The authors declare no conflict of interest.

References

1. Xia, Y.; Zhao, X.; Xia, C.; Wu, Z.-Y.; Zhu, P.; Kim, J.Y.; Bai, X.; Gao, G.; Hu, Y.; Zhong, J.; et al. Highly Active and Selective Oxygen Reduction to H_2O_2 on Boron-Doped Carbon for High Production Rates. *Nat. Commun.* **2021**, *12*, 4225. [CrossRef] [PubMed]
2. Shah, A.U.H.A.; Inayat, A.; Bilal, S. Enhanced Electrocatalytic Behaviour of Poy(Aniline-Co-2-Hydroxyaniline) Coated Electrodes for Hydrogen Peroxide Electrooxidation. *Catalysts* **2019**, *9*, 631. [CrossRef]
3. Song, W.; Zhao, R.; Yu, L.; Xie, X.; Sun, M.; Li, Y. Enhanced Catalytic Hydrogen Peroxide Production from Hydroxylamine Oxidation on Modified Activated Carbon Fibers: The Role of Surface Chemistry. *Catalysts* **2021**, *11*, 1515. [CrossRef]

4. Sun, F.; Yang, C.; Qu, Z.; Zhou, W.; Ding, Y.; Gao, J.; Zhao, G.; Xing, D.; Lu, Y. Inexpensive Activated Coke Electrocatalyst for High-Efficiency Hydrogen Peroxide Production: Coupling Effects of Amorphous Carbon Cluster and Oxygen Dopant. *Appl. Catal. B* **2021**, *286*, 119860. [CrossRef]
5. Huynh, T.-T.; Huang, W.-H.; Tsai, M.-C.; Nugraha, M.; Haw, S.-C.; Lee, J.-F.; Su, W.-N.; Hwang, B.J. Synergistic Hybrid Support Comprising TiO_2–Carbon and Ordered PdNi Alloy for Direct Hydrogen Peroxide Synthesis. *ACS Catal.* **2021**, *11*, 8407–8416. [CrossRef]
6. Pan, C.; Zheng, Y.; Yang, J.; Lou, D.; Li, J.; Sun, Y.; Liu, W. Pt–Pd Bimetallic Aerogel as High-Performance Electrocatalyst for Nonenzymatic Detection of Hydrogen Peroxide. *Catalysts* **2022**, *12*, 528. [CrossRef]
7. Chen, S.; Luo, T.; Chen, K.; Lin, Y.; Fu, J.; Liu, K.; Cai, C.; Wang, Q.; Li, H.; Li, X.; et al. Chemical Identification of Catalytically Active Sites on Oxygen-doped Carbon Nanosheet to Decipher the High Activity for Electro-synthesis Hydrogen Peroxide. *Angew. Chem. Int. Ed.* **2021**, *60*, 16607–16614. [CrossRef] [PubMed]
8. Liu, C.; Li, H.; Chen, J.; Yu, Z.; Ru, Q.; Li, S.; Henkelman, G.; Wei, L.; Chen, Y. 3d Transition-Metal-Mediated Columbite Nanocatalysts for Decentralized Electrosynthesis of Hydrogen Peroxide. *Small* **2021**, *17*, 2007249. [CrossRef] [PubMed]
9. Liu, Y.; Chen, Y.; Deng, J.; Wang, J. N-Doped Aluminum-Graphite (Al-Gr-N) Composite for Enhancing in-Situ Production and Activation of Hydrogen Peroxide to Treat Landfill Leachate. *Appl. Catal. B* **2021**, *297*, 120407. [CrossRef]
10. Wu, Y.; Li, Y.; Gao, J.; Zhang, Q. Recent Advances in Vacancy Engineering of Metal-organic Frameworks and Their Derivatives for Electrocatalysis. *SusMat* **2021**, *1*, 66–87. [CrossRef]
11. Chen, Z.; Chen, S.; Siahrostami, S.; Chakthranont, P.; Hahn, C.; Nordlund, D.; Dimosthenis, S.; Nørskov, J.K.; Bao, Z.; Jaramillo, T.F. Development of a Reactor with Carbon Catalysts for Modular-Scale, Low-Cost Electrochemical Generation of H_2O_2. *React. Chem. Eng.* **2017**, *2*, 239–245. [CrossRef]
12. Li, W.; Bonakdarpour, A.; Gyenge, E.; Wilkinson, D.P. Drinking Water Purification by Electrosynthesis of Hydrogen Peroxide in a Power-Producing PEM Fuel Cell. *ChemSusChem* **2013**, *6*, 2137–2143. [CrossRef] [PubMed]
13. Cao, K.; Yang, H.; Bai, S.; Xu, Y.; Yang, C.; Wu, Y.; Xie, M.; Cheng, T.; Shao, Q.; Huang, X. Efficient Direct H_2O_2 Synthesis Enabled by PdPb Nanorings via Inhibiting the O–O Bond Cleavage in O_2 and H_2O_2. *ACS Catal.* **2021**, *11*, 1106–1118. [CrossRef]
14. Wang, Y.; Waterhouse, G.I.N.; Shang, L.; Zhang, T. Electrocatalytic Oxygen Reduction to Hydrogen Peroxide: From Homogeneous to Heterogeneous Electrocatalysis. *Adv. Energy Mater.* **2021**, *11*, 2003323. [CrossRef]
15. Menegazzo, F.; Signoretto, M.; Ghedini, E.; Strukul, G. Looking for the "Dream Catalyst" for Hydrogen Peroxide Production from Hydrogen and Oxygen. *Catalysts* **2019**, *9*, 251. [CrossRef]
16. Wen, Y.; Li, R.; Liu, J.; Wei, Z.; Li, S.; Du, L.; Zu, K.; Li, Z.; Pan, Y.; Hu, H. A Temperature-Dependent Phosphorus Doping on $Ti_3C_2T_x$ MXene for Enhanced Supercapacitance. *J. Colloid Interface Sci.* **2021**, *604*, 239–247. [CrossRef] [PubMed]
17. Pan, Y.; Abazari, R.; Wu, Y.; Gao, J.; Zhang, Q. Advances in Metal–Organic Frameworks and Their Derivatives for Diverse Electrocatalytic Applications. *Electrochem. Commun.* **2021**, *126*, 107024. [CrossRef]
18. Back, S.; Na, J.; Ulissi, Z.W. Efficient Discovery of Active, Selective, and Stable Catalysts for Electrochemical H_2O_2 Synthesis through Active Motif Screening. *ACS Catal.* **2021**, *11*, 2483–2491. [CrossRef]
19. Hu, Y.; Zhang, J.; Shen, T.; Li, Z.; Chen, K.; Lu, Y.; Zhang, J.; Wang, D. Efficient Electrochemical Production of H_2O_2 on Hollow N-Doped Carbon Nanospheres with Abundant Micropores. *ACS Appl. Mater. Interfaces* **2021**, *13*, 29551–29557. [CrossRef] [PubMed]
20. Jiang, K.; Back, S.; Akey, A.J.; Xia, C.; Hu, Y.; Liang, W.; Schaak, D.; Stavitski, E.; Nørskov, J.K.; Siahrostami, S.; et al. Highly Selective Oxygen Reduction to Hydrogen Peroxide on Transition Metal Single Atom Coordination. *Nat. Commun.* **2019**, *10*, 3997. [CrossRef]
21. Kim, H.W.; Ross, M.B.; Kornienko, N.; Zhang, L.; Guo, J.; Yang, P.; McCloskey, B.D. Efficient Hydrogen Peroxide Generation Using Reduced Graphene Oxide-Based Oxygen Reduction Electrocatalysts. *Nat. Catal.* **2018**, *1*, 282–290. [CrossRef]
22. Zhang, Y.; Lyu, Z.; Chen, Z.; Zhu, S.; Shi, Y.; Chen, R.; Xie, M.; Yao, Y.; Chi, M.; Shao, M.; et al. Maximizing the Catalytic Performance of $Pd@Au_xPd_{1-x}$ Nanocubes in H_2O_2 Production by Reducing Shell Thickness to Increase Compositional Stability. *Angew. Chem. Int. Ed.* **2021**, *60*, 19643–19647. [CrossRef] [PubMed]
23. Mavrikis, S.; Göltz, M.; Perry, S.C.; Bogdan, F.; Leung, P.K.; Rosiwal, S.; Wang, L.; Ponce de León, C. Effective Hydrogen Peroxide Production from Electrochemical Water Oxidation. *ACS Energy Lett.* **2021**, *6*, 2369–2377. [CrossRef]
24. Li, Z.; Zhang, X.; Kang, Y.; Yu, C.C.; Wen, Y.; Hu, M.; Meng, D.; Song, W.; Yang, Y. Interface Engineering of Co-LDH@MOF Heterojunction in Highly Stable and Efficient Oxygen Evolution Reaction. *Adv. Sci.* **2021**, *8*, 2002631. [CrossRef] [PubMed]
25. Li, Z.; Ma, C.; Wen, Y.; Wei, Z.; Xing, X.; Chu, J.; Yu, C.; Wang, K.; Wang, Z.-K. Highly Conductive Dodecaborate/MXene Composites for High Performance Supercapacitors. *Nano Res.* **2020**, *13*, 196–202. [CrossRef]
26. Jung, E.; Shin, H.; Lee, B.-H.; Efremov, V.; Lee, S.; Lee, H.S.; Kim, J.; Hooch Antink, W.; Park, S.; Lee, K.-S.; et al. Atomic-Level Tuning of Co–N–C Catalyst for High-Performance Electrochemical H_2O_2 Production. *Nat. Mater.* **2020**, *19*, 436–442. [CrossRef]
27. Wang, N.; Ma, S.; Zuo, P.; Duan, J.; Hou, B. Recent Progress of Electrochemical Production of Hydrogen Peroxide by Two-Electron Oxygen Reduction Reaction. *Adv. Sci.* **2021**, *8*, 2100076. [CrossRef] [PubMed]
28. Sun, Y.; Silvioli, L.; Sahraie, N.R.; Ju, W.; Li, J.; Zitolo, A.; Li, S.; Bagger, A.; Arnarson, L.; Wang, X.; et al. Activity–Selectivity Trends in the Electrochemical Production of Hydrogen Peroxide over Single-Site Metal–Nitrogen–Carbon Catalysts. *J. Am. Chem. Soc.* **2019**, *141*, 12372–12381. [CrossRef] [PubMed]

29. Sun, Y.; Li, S.; Jovanov, Z.P.; Bernsmeier, D.; Wang, H.; Paul, B.; Wang, X.; Kühl, S.; Strasser, P. Structure, Activity, and Faradaic Efficiency of Nitrogen-Doped Porous Carbon Catalysts for Direct Electrochemical Hydrogen Peroxide Production. *ChemSusChem* **2018**, *11*, 3388–3395. [CrossRef] [PubMed]
30. Naina, V.R.; Wang, S.; Sharapa, D.I.; Zimmermann, M.; Hähsler, M.; Niebl-Eibenstein, L.; Wang, J.; Wöll, C.; Wang, Y.; Singh, S.K.; et al. Shape-Selective Synthesis of Intermetallic Pd_3Pb Nanocrystals and Enhanced Catalytic Properties in the Direct Synthesis of Hydrogen Peroxide. *ACS Catal.* **2021**, *11*, 2288–2301. [CrossRef]
31. Liang, J.; Wang, Y.; Liu, Q.; Luo, Y.; Li, T.; Zhao, H.; Lu, S.; Zhang, F.; Asiri, A.M.; Liu, F.; et al. Electrocatalytic Hydrogen Peroxide Production in Acidic Media Enabled by NiS_2 Nanosheets. *J. Mater. Chem. A* **2021**, *9*, 6117–6122. [CrossRef]
32. Sheng, H.; Hermes, E.D.; Yang, X.; Ying, D.; Janes, A.N.; Li, W.; Schmidt, J.R.; Jin, S. Electrocatalytic Production of H_2O_2 by Selective Oxygen Reduction Using Earth-Abundant Cobalt Pyrite (CoS_2). *ACS Catal.* **2019**, *9*, 8433–8442. [CrossRef]
33. Dong, K.; Liang, J.; Wang, Y.; Xu, Z.; Liu, Q.; Luo, Y.; Li, T.; Li, L.; Shi, X.; Asiri, A.M.; et al. Honeycomb Carbon Nanofibers: A Superhydrophilic O_2-Entrapping Electrocatalyst Enables Ultrahigh Mass Activity for the Two-Electron Oxygen Reduction Reaction. *Angew. Chem. Int. Ed.* **2021**, *60*, 10583–10587. [CrossRef] [PubMed]
34. Li, Z.; Yu, C.; Wen, Y.; Gao, Y.; Xing, X.; Wei, Z.; Sun, H.; Zhang, Y.-W.; Song, W. Mesoporous Hollow Cu–Ni Alloy Nanocage from Core–Shell Cu@Ni Nanocube for Efficient Hydrogen Evolution Reaction. *ACS Catal.* **2019**, *9*, 5084–5095. [CrossRef]
35. Han, G.-F.; Li, F.; Zou, W.; Karamad, M.; Jeon, J.-P.; Kim, S.-W.; Kim, S.-J.; Bu, Y.; Fu, Z.; Lu, Y.; et al. Building and Identifying Highly Active Oxygenated Groups in Carbon Materials for Oxygen Reduction to H_2O_2. *Nat. Commun.* **2020**, *11*, 2209. [CrossRef] [PubMed]
36. Li, Z.; Yu, C.; Kang, Y.; Zhang, X.; Wen, Y.; Wang, Z.-K.; Ma, C.; Wang, C.; Wang, K.; Qu, X.; et al. Ultra-Small Hollow Ternary Alloy Nanoparticles for Efficient Hydrogen Evolution Reaction. *Natl. Sci. Rev.* **2021**, *8*, nwaa204. [CrossRef] [PubMed]
37. Gill, T.M.; Vallez, L.; Zheng, X. The Role of Bicarbonate-Based Electrolytes in H_2O_2 Production through Two-Electron Water Oxidation. *ACS Energy Lett.* **2021**, *6*, 2854–2862. [CrossRef]
38. Naguib, M.; Mashtalir, O.; Carle, J.; Presser, V.; Lu, J.; Hultman, L.; Gogotsi, Y.; Barsoum, M.W. Two-Dimensional Transition Metal Carbides. *ACS Nano* **2012**, *6*, 1322–1331. [CrossRef]
39. Naguib, M.; Kurtoglu, M.; Presser, V.; Lu, J.; Niu, J.; Heon, M.; Hultman, L.; Gogotsi, Y.; Barsoum, M.W. Two-Dimensional Nanocrystals Produced by Exfoliation of Ti_3AlC_2. *Adv. Mater.* **2011**, *23*, 4248–4253. [CrossRef] [PubMed]
40. Anasori, B.; Lukatskaya, M.R.; Gogotsi, Y. 2D Metal Carbides and Nitrides (MXenes) for Energy Storage. *Nat. Rev. Mater.* **2017**, *2*, 16098. [CrossRef]
41. Wen, Y.; Wei, Z.; Liu, J.; Li, R.; Wang, P.; Zhou, B.; Zhang, X.; Li, J.; Li, Z. Synergistic Cerium Doping and MXene Coupling in Layered Double Hydroxides as Efficient Electrocatalysts for Oxygen Evolution. *J. Energy Chem.* **2021**, *52*, 412–420. [CrossRef]
42. Huang, X.; Song, M.; Zhang, J.; Zhang, J.; Liu, W.; Zhang, C.; Zhang, W.; Wang, D. Investigation of MXenes as Oxygen Reduction Electrocatalyst for Selective H_2O_2 Generation. *Nano Res.* **2022**, *15*, 3927–3932. [CrossRef]
43. Wen, Y.; Wei, Z.; Ma, C.; Xing, X.; Li, Z.; Luo, D. MXene Boosted CoNi-ZIF-67 as Highly Efficient Electrocatalysts for Oxygen Evolution. *Nanomaterials* **2019**, *9*, 775. [CrossRef] [PubMed]
44. Nagarajan, R.D.; Sundaramurthy, A.; Sundramoorthy, A.K. Synthesis and Characterization of MXene ($Ti_3C_2T_x$)/Iron Oxide Composite for Ultrasensitive Electrochemical Detection of Hydrogen Peroxide. *Chemosphere* **2022**, *286*, 131478. [CrossRef] [PubMed]
45. Wen, Y.; Ma, C.; Wei, Z.; Zhu, X.; Li, Z. FeNC/MXene Hybrid Nanosheet as an Efficient Electrocatalyst for Oxygen Reduction Reaction. *RSC Adv.* **2019**, *9*, 13424–13430. [CrossRef] [PubMed]
46. Liu, X.; Xu, F.; Li, Z.; Liu, Z.; Yang, W.; Zhang, Y.; Fan, H.; Yang, H.Y. Design Strategy for MXene and Metal Chalcogenides/Oxides Hybrids for Supercapacitors, Secondary Batteries and Electro/Photocatalysis. *Coord. Chem. Rev.* **2022**, *464*, 214544. [CrossRef]
47. Peng, J.; Chen, X.; Ong, W.-J.; Zhao, X.; Li, N. Surface and Heterointerface Engineering of 2D MXenes and Their Nanocomposites: Insights into Electro- and Photocatalysis. *Chem* **2019**, *5*, 18–50. [CrossRef]
48. Zhang, J.; Zhao, Y.; Guo, X.; Chen, C.; Dong, C.-L.; Liu, R.-S.; Han, C.-P.; Li, Y.; Gogotsi, Y.; Wang, G. Single Platinum Atoms Immobilized on an MXene as an Efficient Catalyst for the Hydrogen Evolution Reaction. *Nat. Catal.* **2018**, *1*, 985–992. [CrossRef]
49. Tang, Q.; Zhou, Z.; Shen, P. Are MXenes Promising Anode Materials for Li Ion Batteries? Computational Studies on Electronic Properties and Li Storage Capability of Ti_3C_2 and $Ti_3C_2X_2$ (X = F, OH) Monolayer. *J. Am. Chem. Soc.* **2012**, *134*, 16909–16916. [CrossRef]
50. Xu, S.; Wei, G.; Li, J.; Han, W.; Gogotsi, Y. Flexible MXene–Graphene Electrodes with High Volumetric Capacitance for Integrated Co-Cathode Energy Conversion/Storage Devices. *J. Mater. Chem. A* **2017**, *5*, 17442–17451. [CrossRef]
51. Li, Y.; Ding, L.; Guo, Y.; Liang, Z.; Cui, H.; Tian, J. Boosting the Photocatalytic Ability of g-C_3N_4 for Hydrogen Production by Ti_3C_2 MXene Quantum Dots. *ACS Appl. Mater. Interfaces* **2019**, *11*, 41440–41447. [CrossRef] [PubMed]
52. Yilmaz, G.; Yam, K.M.; Zhang, C.; Fan, H.J.; Ho, G.W. In Situ Transformation of MOFs into Layered Double Hydroxide Embedded Metal Sulfides for Improved Electrocatalytic and Supercapacitive Performance. *Adv. Mater.* **2017**, *29*, 1606814. [CrossRef]
53. Zhu, Y.; Li, X.; Zhang, D.; Bao, H.; Shu, Y.; Guo, X.; Yin, Y. Tuning the Surface Charges of MoO_3 by Adsorption of Polyethylenimine to Realize the Electrophoretic Deposition of High-Exothermic Al/MoO_3 Nanoenergetic Films. *Mater. Des.* **2016**, *109*, 652–658. [CrossRef]
54. Liu, H.; Lv, T.; Zhu, C.; Zhu, Z. Direct Bandgap Narrowing of TiO_2/MoO_3 Heterostructure Composites for Enhanced Solar-Driven Photocatalytic Activity. *Sol. Energy Mater. Sol. Cells* **2016**, *153*, 1–8. [CrossRef]

55. Matsui, H.; Nagano, S.; Karuppuchamy, S.; Yoshihara, M. Synthesis and Characterization of TiO_2/MoO_3/Carbon Clusters Composite Material. *Curr. Appl. Phys.* **2009**, *9*, 561–566. [CrossRef]
56. Maughan, P.A.; Bouscarrat, L.; Seymour, V.R.; Shao, S.; Haigh, S.J.; Dawson, R.; Tapia-Ruiz, N.; Bimbo, N. Pillared Mo_2TiC_2 MXene for High-Power and Long-Life Lithium and Sodium-Ion Batteries. *Nanoscale Adv.* **2021**, *3*, 3145–3158. [CrossRef] [PubMed]
57. Regue, M.; Armstrong, K.; Walsh, D.; Richards, E.; Johnson, A.L.; Eslava, S. Mo-Doped TiO_2 Photoanodes Using $[Ti_4Mo_2O_8(OEt)_{10}]_2$ Bimetallic Oxo Cages as a Single Source Precursor. *Curr. Appl. Phys.* **2018**, *2*, 2674–2686. [CrossRef]
58. Dixit, D.; Ramachandran, B.; Chitra, M.; Madhuri, K.V.; Mangamma, G. Photochromic Response of the PLD-Grown Nanostructured MoO_3 Thin Films. *Appl. Surf. Sci.* **2021**, *553*, 149580. [CrossRef]
59. Liu, H.; Cai, Y.; Han, M.; Guo, S.; Lin, M.; Zhao, M.; Zhang, Y.; Chi, D. Aqueous and Mechanical Exfoliation, Unique Properties, and Theoretical Understanding of MoO_3 Nanosheets Made from Free-Standing α-MoO_3 Crystals: Raman Mode Softening and Absorption Edge Blue Shift. *Nano Res.* **2018**, *11*, 1193–1203. [CrossRef]
60. Siahrostami, S.; Verdaguer-Casadevall, A.; Karamad, M.; Deiana, D.; Malacrida, P.; Wickman, B.; Escudero-Escribano, M.; Paoli, E.A.; Frydendal, R.; Hansen, T.W.; et al. Enabling Direct H_2O_2 Production through Rational Electrocatalyst Design. *Nat. Mater.* **2013**, *12*, 1137–1143. [CrossRef]
61. Ye, Y.-X.; Wen, C.; Pan, J.; Wang, J.-W.; Tong, Y.-J.; Wei, S.; Ke, Z.; Jiang, L.; Zhu, F.; Zhou, N.; et al. Visible-Light Driven Efficient Overall H_2O_2 Production on Modified Graphitic Carbon Nitride under Ambient Conditions. *Appl. Catal. B* **2021**, *285*, 119726. [CrossRef]